



Improving the performance of destructive interference phononic crystal structure through topology optimization

Tam Yee Ha, Gil Ho Yoon *

School of Mechanical Engineering, Hanyang University, Seoul, South Korea

ARTICLE INFO

Keywords:

Topology optimization
Destructive interference
Resonance phenomenon
Metamaterials
Phononic crystals

ABSTRACT

This study examines the phenomenon of intrinsic nature in wave mitigation, specifically focusing on the concept of destructive interference (DI). When waves interact, they can exhibit either destructive interference or constructive interference depending on the phase difference. In the case of mechanical waves propagating through a mechanical structure, their characteristics such as wave speed, wavelength, and wave attenuation are influenced by the properties of the structure. As waves travel within the structure, the resonance phenomenon of the mechanical structure induces a phase shift of approximately 180 degrees in the wave. Consequently, what was initially destructive interference can transit into constructive interference, and vice versa. To address this challenge and systematically enhance the performance of mechanical structures employing destructive interference, a topology optimization scheme is applied. The concept of the present optimization scheme and the advantages are highlighted for several in-plane vibrations.

1. Introduction

This paper investigates the effect of the resonance of the destructive interference (DI) structure and presents an application of topology optimization to improve the dynamic performance of the triangular shaped destructive interference structure which can be observed when a wave encounters another wave. Depending on the phase difference, the wave undergoes either destructive interference or constructive interference. In the case of mechanical waves, which commonly propagate through elastic body, their characteristics such as wave speed, wavelength, or wave attenuation depend on the properties of elastic body. Utilizing these characteristics, it becomes possible to control the wave. For an example, Fig. 1(a) shows a real engineering project of Incremental Unitary Envelope System (IUES) that integrates various pieces of equipment and renewable energy technologies in South Korea to improve the building energy efficiency. In this project, assigned task is to design elastic metamaterials with effective vibration attenuation performance within the frequency range of vibrations. A heat pump is installed at the glass window and it is necessary to reduce the effects of the vibration caused by the heat pump. To attenuate the vibration, the triangular shape phononic crystal (PC) is installed beneath the heat pump. Due to the destructive interference of the triangular shape structure, it is possible to effectively attenuate the vibration. However, as mechanical wave travels within mechanical structure, it interacts with the structure's resonance phenomenon, causing a shift in the phase of the wave by approximately 180 degrees as shown in Fig. 1((b)-center). It is intriguing to note that what was once destructive interference can transform into constructive interference, and vice versa, due to this interaction. To overcome the challenges posed by this phenomenon and to enhance the performance of mechanical structures with destructive interference systematically, the topology optimization scheme is applied in this study.

* Correspondence to: Department of Mechanical Engineering, College of Engineering, Hanyang University, Seoul, South Korea.
E-mail address: ghy@hanyang.ac.kr (G.H. Yoon).

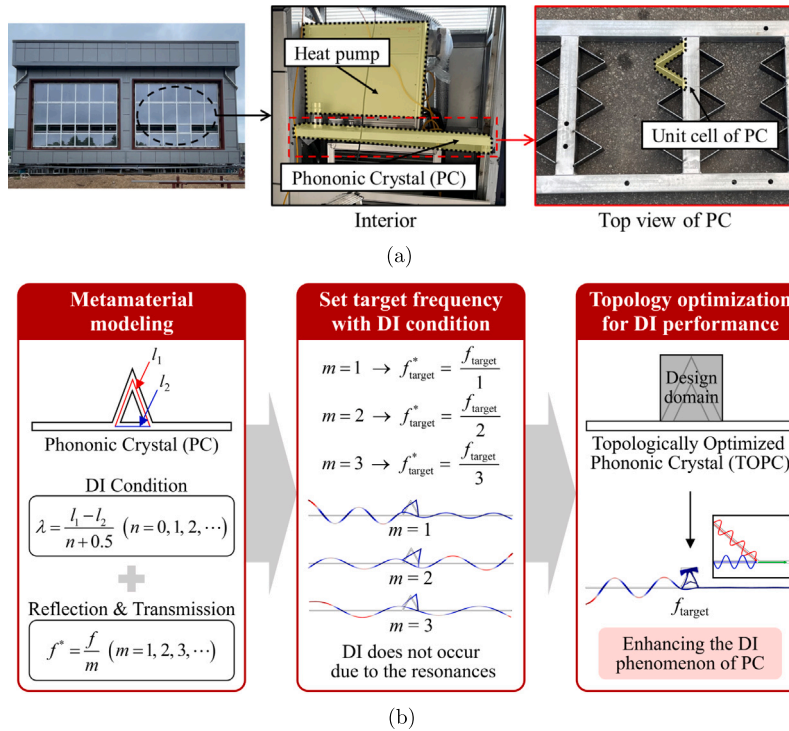


Fig. 1. (a) A real building project with the triangular shaped destructive interference structure attenuating vibration caused by the heat pump and (b) the research objective.

Several innovative researches exist for the emerging area of metamaterials, phononic and photonic crystals to attenuate or control elastic wave, acoustic wave and electromagnetic wave [1–9]. In addition, several innovative approaches exist for controlling wave propagation and bandgap. There exist diverse methods for controlling wave propagation and creating bandgap structures. In [10], it is demonstrated that wide and robust bandgaps can be established by combining the formation of Bragg scattering and local resonances. In [11], the wave attenuation and wide bandgaps are investigated by coupling the mechanisms of Bragg scattering and local resonance in a viscoelastic phononic crystal rod with periodic dissipative resonators. In [12], the mechanism of the ultra-wide bandgap is investigated based on the rigid body resonance of a periodic hexagonal lattice. In [13], the low-frequency bandgap is investigated through the rigid body resonance of a phononic crystal composed of a simple combination of traditional phononic crystals. In [14], the locally resonant phononic crystals appear the low frequency bandgap using the Bloch theorem. On the other hand, one notable approach here is based on the principle of destructive interference. The acoustic metamaterial (AM) is analyzed using a spectral element method, demonstrating the coexistence of destructive interference and local resonance mechanisms for attenuating elastic wave propagation [15]. A phononic crystal consisting of hourglass-shaped periodic lattice resonators is presented. The bandgap is formed with effective mechanical properties through an hourglass lattice design featuring a central cubic resonator mass [16]. In [17], a metasurface is designed using the destructive interference method to control the propagation of seismic surface waves. The arrangement and gradient indexing design enable the creation of an ultra-wide bandgap. In [18], the concept of destructive interference and gradient-index phononic crystals are presented for controlling shear wave propagation with a broad bandgap. Furthermore, there are studies that have implemented the destructive interference mechanism with phase difference [19,20]. In [19], a piezoelectric phononic crystal plate that attenuates elastic waves using destructive interference by considering the phase difference is reported. A phononic crystal with coupled lanes is proposed for elastic wave attenuation, designed to achieve destructive interference by controlling the phase difference of split parts of these lanes in [20].

To enhance the characteristics of phononic crystals and achieve wide bandgaps, optimization methods are employed, utilizing either gradient-based or non-gradient-based optimization techniques. Non-gradient-based optimization is primarily implemented using the genetic algorithm (GA), which is advantageous for multi-objective optimization and global optimum search [21,22]. An optimization method based on GA is presented to have a lower longitudinal modulus of acoustic and elastic phononic crystals in [21]. In [22], multi-objective optimization is performed using GA to achieve maximum bandgap and minimum mass in porous phononic crystals. On the other hand, research has also been conducted on gradient-based algorithms with fast convergence rates and clear termination criteria [23–30]. In [23], the gradient-based bi-directional evolutionary structural optimization (BESO) method was proposed to maximize the bandgap of 2D solid hexagonal-latticed phononic crystals. In [24], the optimization results of dielectric elastomers with gradient-based optimization and genetic algorithms (GA) are compared. In [25], the gradient-based and non-gradient-based topology optimization methods of phononic crystals and the bandgap structure of phononic crystal are reviewed.

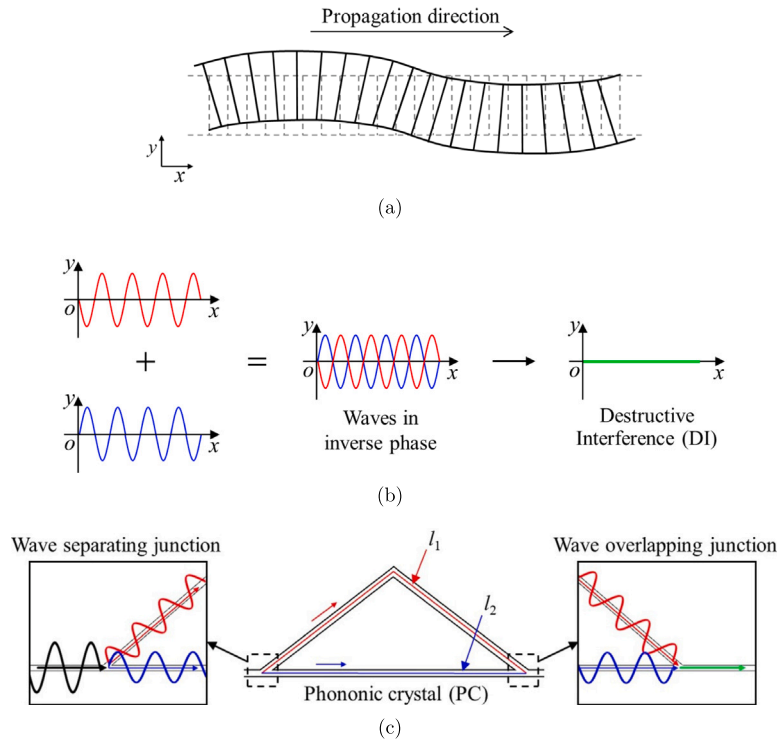


Fig. 2. (a) Wave propagation, (b) destructive interference and (c) a phononic crystal using destructive interference.

In [26], an optimization for wave control through the bandgap of the periodic elastic structure is presented and the optimization result is verified through experiments. In [27], the finite element analysis is conducted with Bloch-Floquet theory, and the main objective is to maximize the width of elastic wave bandgaps in piezocomposite materials using topology optimization. In [28], the feature-driven joint topology optimization is employed to design phononic crystal with a broad bandgap through localized resonance and to achieve negative refraction. Additionally, there exist previous studies on phase optimization aiming at controlling the phase of waves. In [31], a density-based topology optimization method is formulated to find phase-delaying unit cells suitable for forming a metasurface that anomalously reflects longitudinal waves. Each unit cell generates a specific phase delay between oncoming and reflected elastic waves. In [32], a GA-based topology optimization formulation is proposed to achieve specific phase delay and high transmission.

The present study considers the destructive interference of the triangular shape structure which is tailored to improve the transverse vibration attenuation at target frequencies. The proposed DI structure offers a notable advantage in ease of implementation by adjusting only the path length difference to achieve destructive interference. Additionally, observation of destructive interference is possible even at low frequencies due to the reflection and transmission of mechanical wave. Although the destructive interference of elastic wave can be utilized, the resonance frequencies of the triangular shape structure prevents the destructive interference of transverse vibration. Despite the basic destructive interference structure is designed by the physics law, the mechanical vibrations at specific frequencies remain challenging to suppress. As shown in Fig. 1(b), the present study applies a topology optimization scheme to investigate and improve vibration attenuation performance. The Young's modulus and the density of finite elements are interpolated with respect to the spatially varying design variables and the penalization factor of the mass matrix is higher than that of the stiffness matrix to prevent the local mode issue. The transverse vibrations at the output domain are set to the objective function. By topology optimization, an improved destructive interference structure can be systematically found. The effectiveness of the optimized structure is tested.

The remainder of this paper is organized as follows. Section 2 provides the mathematical formula of structural analysis and the development of the sensitivity analysis of the DI based phononic crystal (PC). Section 3 describes several topology optimization examples. Section 4 presents the conclusions of the study and provides suggestions for future research.

2. Destructive interference and topology optimization formulation

2.1. Theory for transverse vibration and destructive interference

The present study considers the transverse vibration whose propagation direction is perpendicular to the direction of the displacement as shown in Fig. 2(a). Indeed, in [33], it reviews the transverse vibration of axially moving strings and investigates

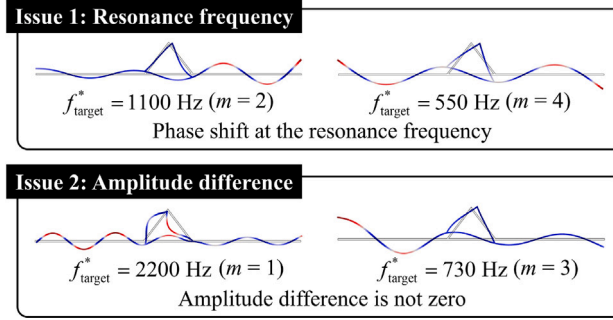


Fig. 3. Issues of DI structure: Example of the phononic crystal with $l_1 = 0.072$ m, $l_2 = 0.118$ m and $f_{\text{target}} = 2200$ Hz.

the control of the vibrations. In [34], the transverse wave propagation of functionally graded Euler nanobeams and their vibration behavior is investigated. The destructive interference phenomenon is widely known and it becomes an issue in real applications to have waves and shifted waves. To achieve this destructive interference, this research presented the triangular shape as shown in Fig. 2(c), with the long and short paths of the DI structure are denoted by l_1 and l_2 .

The beam transverse vibration neglecting the in-plane deformation of structure can be formulated with the following 4-th order differential governing equation of bending wave as follows:

$$EI \frac{\partial^4 \Psi_t(x, t)}{\partial x^4} - \rho A \frac{\partial^2 \Psi_t(x, t)}{\partial t^2} = 0 \quad (1)$$

where the transverse deflection at position x and time t is denoted by $\Psi_t(x, t)$. The density, the cross sectional area, Young's modulus and moment of inertia are denoted by ρ , A , E and I , respectively.

To investigate the vibration of the beam, we assume the harmonic solution as follows:

$$\Psi_t(x, t) = \Psi(x) e^{i\omega t} \quad (2)$$

where the transverse displacement is denoted by $\Psi(x)$. Through variable separation, the equation in (1) can be defined as a harmonic differential equation involving $\Psi(x)$ as follows:

$$\frac{\partial^4 \Psi(x)}{\partial x^4} - k^4 \Psi(x) = 0, \quad k = \omega^{\frac{1}{2}} \left(\frac{\rho A}{EI} \right)^{\frac{1}{4}}, \quad c = \omega^{\frac{1}{2}} \left(\frac{EI}{\rho A} \right)^{\frac{1}{4}} \quad (3)$$

From the dispersion relationship in [35–37], the wave vector becomes dependent on the angular velocity, ω . As the wave vector becomes dependent on the angular velocity $k = \omega/c$, the speed of bending wave c is also dependent on the angular velocity. The elastic bending wavelength is formulated based on the theory of Euler–Bernoulli beam as follows:

$$\lambda = 2\pi\omega^{-\frac{1}{2}} \left(\frac{Eh^2}{12\rho} \right)^{\frac{1}{4}} \quad (4)$$

where the height of structure is denoted by h . Considering the angular velocity and the material properties, the length difference causing the destructive interference can be set as follows:

$$\delta = l_1 - l_2 = \left(n + \frac{1}{2} \right) \lambda, \quad (n = 0, 1, 2, \dots) \quad (5)$$

Consequently, the target frequency f_{target} at which the DI structure operates can be expressed in relation to the paths of wave propagation.

$$f_{\text{target}} = 2\pi \left(\frac{n + 0.5}{l_1 - l_2} \right)^2 \left(\frac{Eh^2}{12\rho} \right)^{\frac{1}{2}} \quad (6)$$

Considering the reflection and transmission of transverse waves, the DI structure can attenuate mechanical waves at other frequencies obtained by dividing the target frequency f_{target} by an integer m .

$$f_{\text{target}}^* = \frac{f_{\text{target}}}{m}, \quad (m = 1, 2, 3, \dots) \quad (7)$$

The benefits of destructive interference lie in the fact that multiple frequencies satisfying the DI condition can be passively suppressed. In addition, the DI structure does not rely on the resonance phenomenon, making it stable from an engineering point of view.

For the dynamic simulation of PC, the finite element procedure is applied. The system equation is formulated as follows:

$$\mathbf{S}\mathbf{X} = (\mathbf{K} - \omega^2 \mathbf{M})\mathbf{X} = \mathbf{F} \quad (8)$$

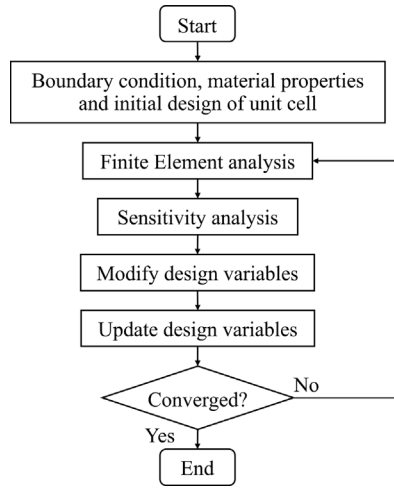


Fig. 4. Optimization procedure.

where the dynamic stiffness matrix, the stiffness matrix and the mass matrix are denoted by \mathbf{S} , \mathbf{K} and \mathbf{M} , respectively. The responses and the force vector are denoted by \mathbf{X} and \mathbf{F} , respectively. The stiffness matrix and the mass matrix are formulated as follows:

$$\mathbf{K} = \sum_{e=1}^{N_e} \mathbf{k}_e, \quad \mathbf{M} = \sum_{e=1}^{N_e} \mathbf{m}_e \quad (9)$$

$$\mathbf{k}_e = \int_v \mathbf{B}^T \mathbf{D} \mathbf{B} dv, \quad \mathbf{m}_e = \int_v \rho_e \mathbf{N}^T \mathbf{N} dv \quad (10)$$

$$\mathbf{D} = \frac{E}{(1-\nu^2)} \begin{bmatrix} 1 & \nu & 0 \\ \nu & 1 & 0 \\ 0 & 0 & \frac{1-\nu}{2} \end{bmatrix} \quad (11)$$

where the e th element stiffness matrix and the e th element mass matrix are denoted by \mathbf{k}_e and \mathbf{m}_e , respectively. The number of finite element is N_e . The shape function matrix, the strain–displacement matrix and the plane-stress element constitutive matrix are denoted by \mathbf{N} , \mathbf{B} and \mathbf{D} , respectively. The density of the e th element is denoted by ρ_e . The Young's modulus and the Poisson's ratio are denoted by E and ν , respectively. By solving the governing equation, the performance of DI structure is analyzed.

2.2. Topology optimization formulation

Based on the above equations, the geometry and the target frequencies of a DI phenomenon should be determined. Nevertheless, as the transverse wave is only considered, some limitations exist as shown in Fig. 3. First of all, the phase shift occurs due to the resonance frequency. Therefore, this causes the side effect that the two waves experience the constructive interference rather than the destructive interference. Another issue is that the amplitude difference of the two transverse waves at the junction deteriorates the performance of the phononic crystal. Therefore, this research aims to improve the performance of the DI structure by the topology optimization.

For the topology optimization, the Solid Isotropic Material with Penalization (SIMP) approach is used for the interpolation of the stiffness matrix and the mass matrix as follows:

$$\mathbf{k}_e = \gamma_e^3 \mathbf{k}_{\text{nominal}}, \quad \mathbf{m}_e = \gamma_e^5 \mathbf{m}_{\text{nominal}} \quad (12)$$

where the nominal stiffness matrix and nominal mass matrix are denoted by $\mathbf{k}_{\text{nominal}}$ and $\mathbf{m}_{\text{nominal}}$, respectively.

To improve the attenuation performance of the DI structure, the following optimization formulation and the procedure in Fig. 4 are developed and considered in this study.

$$\begin{aligned} & \text{Min}_{\gamma} \quad \Phi(\gamma, \mathbf{X}) = |\mathbf{L}^T \mathbf{X}| \\ & \text{Subject to} \quad \mathbf{S} \mathbf{X} = \mathbf{F} \\ & \sum_{e=1}^{N_e} \gamma_e v_e - V_f \leq 0, \\ & \gamma_{\min} \leq \gamma \leq 1, \quad \gamma_{\min} = 0.001 \\ & \gamma = [\gamma_1, \gamma_2, \dots, \gamma_{N_e}] \end{aligned} \quad (13)$$

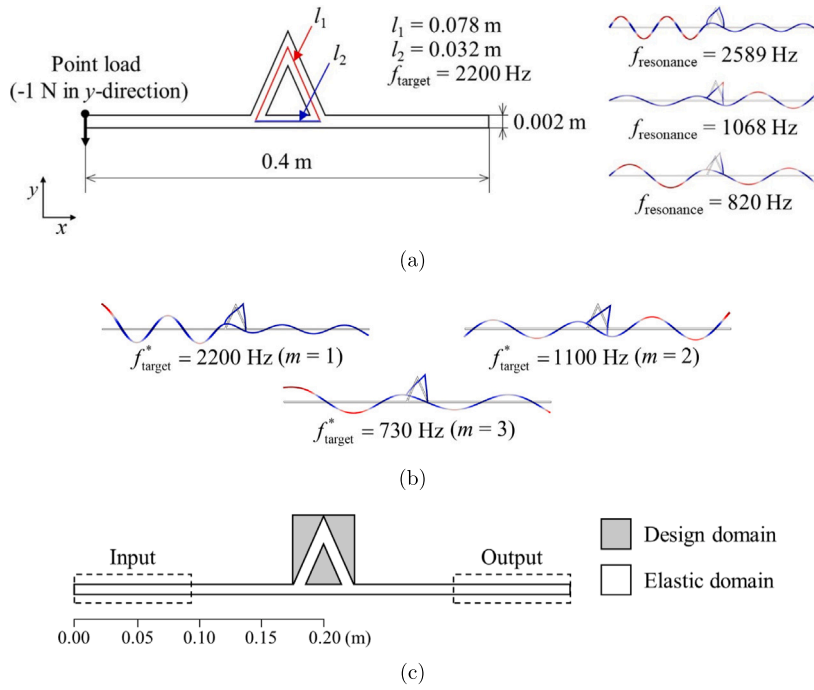


Fig. 5. Example 1: Destructive interference with a triangular shape structure. (a) (left) A model definition ($E = 70$ GPa, $\rho = 2700$ kg/m³, $\nu = 0.33$, thickness = 0.002 m, $f_{\text{target}} = 2200$ Hz, a point load boundary condition -1 N in y direction and free boundary conditions on the remaining sides) and (right) the resonance frequencies of the phononic crystal, (b) wave propagation with $f_{\text{target}}^* = f_{\text{target}}/m$ ($m = 1, 2$ and 3) and (c) the design domain.

where the objective function is denoted by Φ which is a function with the response \mathbf{X} . The vector which returns the displacement values at the output nodes of interest is denoted by \mathbf{L} . The entities of this vector \mathbf{L} are zeros except the corresponding elements associated with the output displacements. The dynamic stiffness matrix is denoted by \mathbf{S} . The mass constraint is imposed with the allowable mass bound. The number of finite elements is N_e . The design variables ranging from γ_{\min} to one are denoted by γ_e .

To obtain the sensitivity analysis of the objective function, the adjoint sensitivity is derived with the following Lagrangian function Φ_L .

$$\Phi_L(\gamma, \mathbf{X}) = \Phi(\gamma, \mathbf{X}) + \lambda^T (\mathbf{S}\mathbf{X} - \mathbf{F}) \quad (14)$$

where the Lagrange multipliers is denoted by λ . By differentiating the above Lagrangian function, the following formulations can be obtained.

$$\begin{aligned} \frac{\partial \Phi_L}{\partial \gamma_e} &= \lambda^T \frac{\partial \mathbf{S}}{\partial \gamma_e} \mathbf{X} \\ &= -\frac{1}{\Phi} (\mathbf{L}^T \mathbf{X}) (\mathbf{S}^{-1} \mathbf{L})^T \frac{\partial \mathbf{S}}{\partial \gamma_e} \mathbf{X} \end{aligned} \quad (15)$$

$$\lambda^T \mathbf{S} = -\frac{1}{\Phi} (\mathbf{L}^T \mathbf{X}) \mathbf{L}^T \quad (16)$$

3. Optimization examples

This section presents several optimization examples and analyses for the destructive interference system. The method of moving asymptotes (MMA) algorithm is employed as an optimization algorithm [38].

3.1. Example 1: DI structure design

3.1.1. DI structure design at single frequency (2200 Hz)

First of all, the triangular shape destructive interference structure in Fig. 5 is devised considering the condition of the destructive interference. Without the loss of generality, the target frequency of the DI is set to 2200 Hz with $m = 1$ as shown in Fig. 5(a)-left. With only considering the DI conditions, the attenuation frequencies become to 2200 Hz, 1100 Hz and 730 Hz depending on the value of m , respectively. However, the FE simulation results show the opposite results or the constructive interference at 1100 Hz as shown in 5(b). Furthermore, the attenuation performance of the mechanical wave degrades even at 2200 Hz and 730 Hz. By investigating the resonance frequencies, it is clear that performance degradation and this constructive interference occur instead of

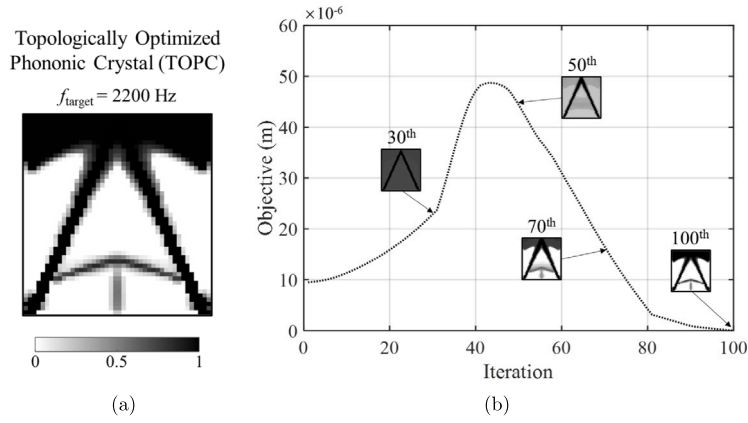


Fig. 6. (a) Layout of TOPC that $f_{\text{target}} = 2200$ Hz and (b) the objective history with the convergence curve, including some intermediate layouts.

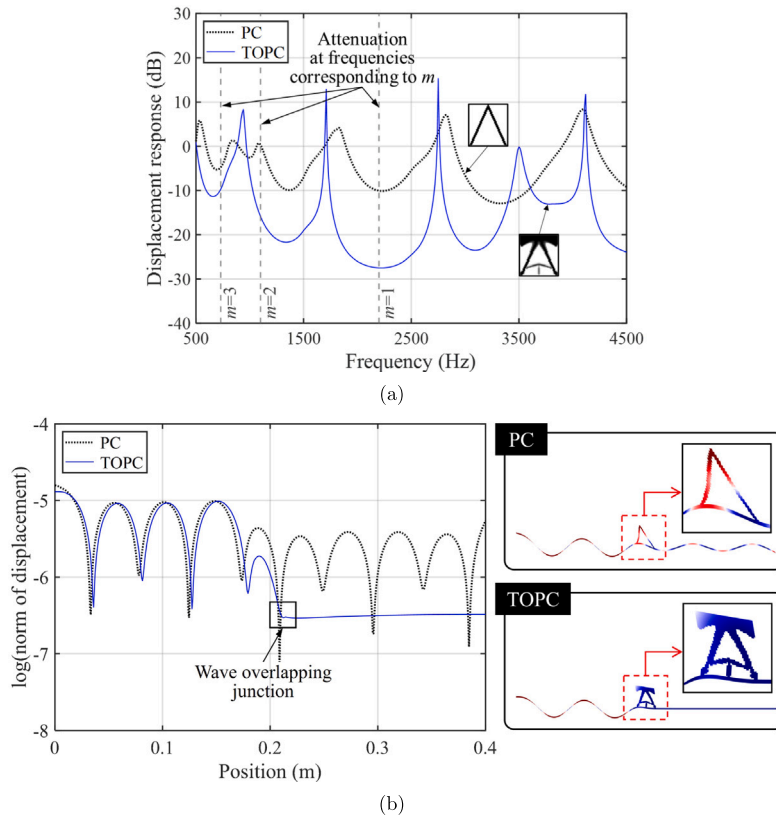


Fig. 7. (a) The displacement response curves of the PC and the TOPC and (b) (left) the norm of displacements curves along the straight beam and (right) the wave propagations of the PC and TOPC at $f_{\text{target}} = 2200$ Hz.

the destructive interference when the targeting frequencies are close to those of the resonance frequencies as shown in Fig. 5(a)-right). The results in Fig. 5(a) and (b) clearly illustrate that due to the effect of the resonance frequencies, the phase becomes shifted. To resolve this side effect systematically and improve the performance of the DI structure, the rectangular domain in Fig. 5(c) is set as the design domain. The objective function is computed by calculating the integration of the transverse displacement at the objective output area which is the end of the right bar as discussed in (13).

Fig. 6(a) shows an optimized layout by solving the optimization problem with 30% mass constraint and Fig. 6(b) shows the convergence curve with some intermediate layouts. There is a hat shaped structure at the upper part of the design domain and

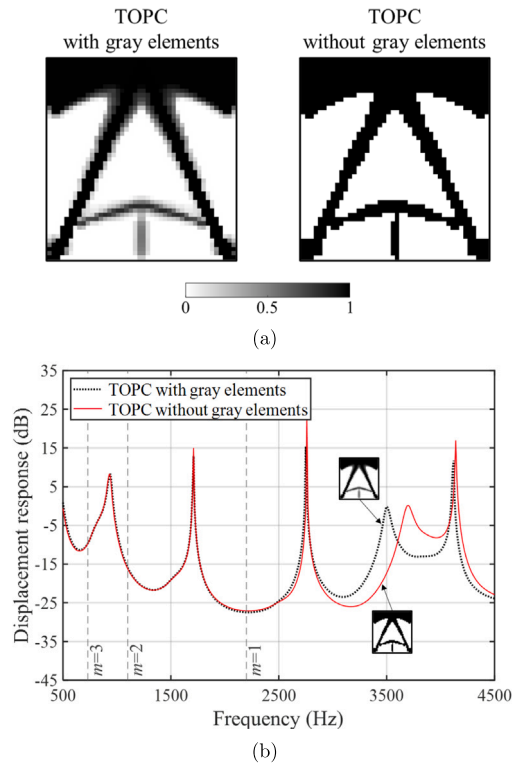


Fig. 8. (a) Layouts of TOPC with and without gray elements and (b) the displacement response curves of the TOPC with and without gray elements.

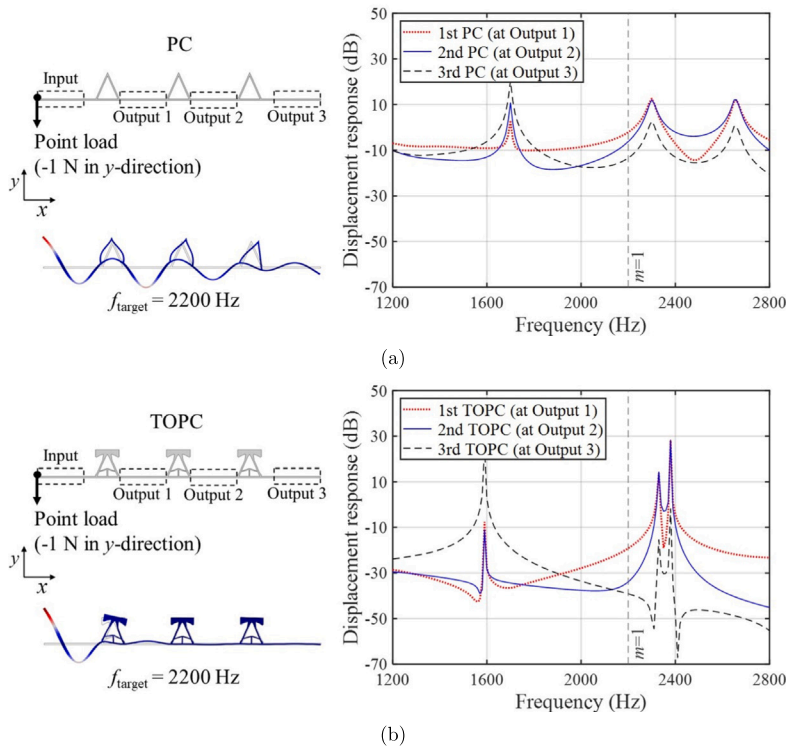


Fig. 9. The effect of the number of the unit structure. (a) Triangular unit cell (PC) and its response and (b) the optimized structure (TOPC) and its response.

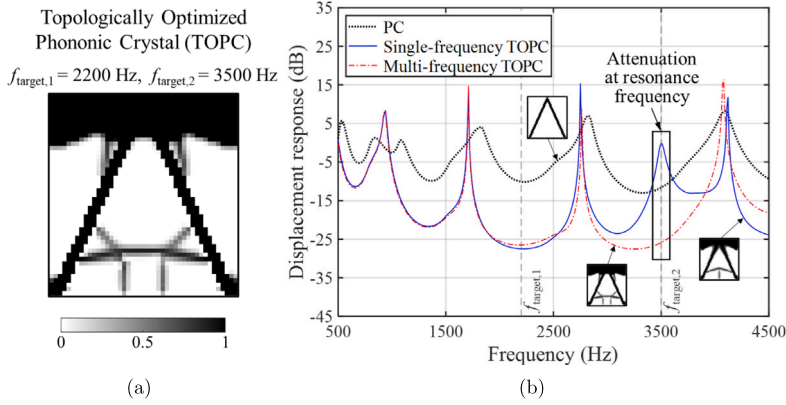


Fig. 10. (a) Layout of TOPC that $f_{\text{target},1} = 2200$ Hz, $f_{\text{target},2} = 3500$ Hz and (b) the displacement response curves of the PC and the TOPCs.

the fork shaped structure appears at the bottom of the design domain whose role is to resist the deflection of the two main supporting bars. The upper hat shape structure plays as an additional mass to the structure and the fork shaped structure increases the stiffness of the eigenmodes oscillating in the side. Fig. 7(a) shows the comparison of the response curves of the original PC and the topologically optimized PC (TOPC). This comparison clearly shows that the optimization process can significantly improve the vibration attenuation function of the destructive interference. For Fig. 7(a), the displacement response is computed as follows:

$$\text{Displacement response (dB)} = 20 \log_{10} \frac{\iint_{\Omega_o} |u_{y,o}| d\Omega_o}{\iint_{\Omega_i} |u_{y,i}| d\Omega_i} \quad (17)$$

where the area of the input domain, Ω_i , is equal to the area of the output domain, Ω_o . The displacements in y direction for the input and output areas are denoted by $u_{y,i}$ and $u_{y,o}$, respectively. One of the interesting points here is that the responses at the other target frequencies, such as $f_{\text{target}}^* = 1100$ Hz ($m = 2$) and $f_{\text{target}}^* = 730$ Hz ($m = 3$), are also significantly minimized by optimizing for $f_{\text{target}} = 2200$ Hz ($m = 1$). The norm curves along the straight beam of the PC and the TOPC at $f_{\text{target}} = 2200$ Hz are shown in Fig. 7(b)-left). It definitely shows that the responses are reduced significantly. The magnified vibrating shapes of the original PC and the optimized TOPC at $f_{\text{target}} = 2200$ Hz are shown in Fig. 7(b)-right). Upon examining the wave propagation, the phase difference becomes almost 180 degrees at the wave overlapping junction of TOPC. The influence of the finite elements with intermediate densities needs to be investigated. To obtain a layout without the elements with the intermediate density values, the optimized design is manually postprocessed to have the clear black-white design in Fig. 8(a). The responses before and after the postprocessing are compared in Fig. 8(b). It turns out that the overall responses are similar across all target frequencies, although there is some discrepancy in the response at higher excitation frequencies. It should be mentioned that without the initial triangular structure, it is impossible to find out the optimized shape in Fig. 6. To the best of our knowledge, this is partially attributed to the local optima issue or the feasibility problem in topology optimization. The optimized structure can be manufactured using advanced manufacturing techniques. The present study can be extended with the topology optimization with the explicit curve or surface such as the level-set method [39–41], the phase-field approaches [42–44] or the MMC(Moving Morphable Component) [45–47].

The responses are computed and compared by increasing the number of the unit cell in Fig. 9(a)-left) and Fig. 9(b)-left). The displacements response for each output area (output 1, 2, 3) are calculated similarly to the equation in (17). The unit force is applied at the left side and the responses at the three outputs are compared; the responses are integrated inside the dotted boxes. As shown here, the more triangular-shaped DI structures are added, the greater the attenuation achieved. The performance of the topological optimized DI structure is superior to the triangular-shaped DI structure, as shown in Fig. 9 that show one of the contributions of the present study.

3.1.2. DI structure design at multiple frequencies (2200 Hz and 3500 Hz)

By investigating the frequency response function of Fig. 7(a), it is observed that the response at 3500 Hz becomes high due to the resonance of the optimized structure that is the side effect of the topology optimization. Indeed, to show the potential of the present approach, this subsection aims to reduce the peaks at 2200 Hz and 3500 Hz simultaneously. With the present approach, the sum of the responses at 2200 Hz and 3500 Hz is considered and the optimized layout in Fig. 10(a) is obtained. The overall layout is similar. See that the head mass appears with some differences in the supporting structures. The response of Fig. 10(b) shows the responses of the triangular shape PC, the optimized layout in Fig. 6(a) and the optimized layout in Fig. 10(a). The responses show that the displacement response of Fig. 7(a) is the lowest at $f_{\text{target},1} = 2200$ Hz with a higher response at $f_{\text{target},2} = 3500$ Hz. However, the responses of Fig. 10(b) at $f_{\text{target},1} = 2200$ Hz and $f_{\text{target},2} = 3500$ Hz are simultaneously lowered (The response of Fig. 10(b) is higher than that of Fig. 7(a) at $f_{\text{target},1} = 2200$ Hz.). Fig. 11 compares the deformations of the three designs at the two target frequencies.

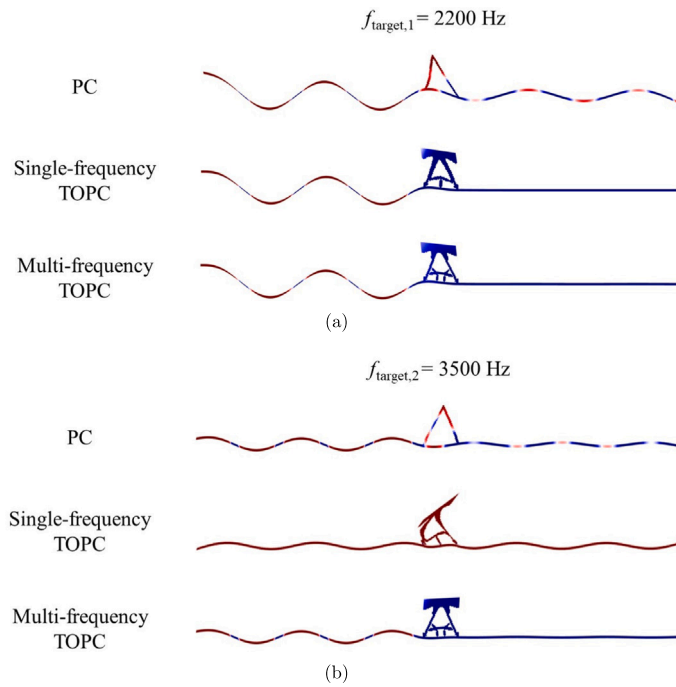


Fig. 11. The wave propagations of the PC, the single-frequency TOPC and the multi-frequency TOPC at (a) $f_{\text{target},1} = 2200$ Hz and (b) $f_{\text{target},2} = 3500$ Hz.

Table 1

Displacement response and amplitude difference along the path of PC and TOPC at $f_{\text{target},2} = 3500$ Hz.

Model	$\max \sqrt{u_x^2 + u_y^2}$		Amplitude difference ($l_1 : l_2$)
	Long path (l_1)	Short path (l_2)	
PC	3.186×10^{-12}	5.580×10^{-13}	5.710 : 1
Single-frequency TOPC	2.855×10^{-9}	4.303×10^{-11}	66.349 : 1
Multi-frequency TOPC	9.435×10^{-14}	1.989×10^{-14}	4.744 : 1

Table 1 compares the maximum displacement of the long path and the short path of the three designs at 3500 Hz. The normalized displacements being compared, by considering the magnitudes of the paths, it turns out that as the PC structure has the different magnitudes at the two paths that explains the large amplitude after the PC structure. The layout in [Fig. 6\(a\)](#) optimized for 2200 Hz shows the different amplitudes in the two paths that also explains the deterioration in terms of the response. However, the layout in [Fig. 10\(a\)](#) decreases the amplitude difference with the same phase as the PC structure. This aspect can be observed in [Fig. 11\(b\)](#) and **Table 1**. **Table 1** explains the vibration attenuation at 3500 Hz depicted in [Fig. 10\(b\)](#), revealing a PC ratio of 5.710:1. However, the ratio of the design optimized at 2200 Hz is 66.349:1 that explains the low performance in the vibration attenuation. By considering the responses at 2200 Hz and 3500 Hz simultaneously, this ratio becomes 4.744:1 that enhances the vibration attenuation. As illustrated, the figures and the table clearly show the applicability of the present approach.

3.1.3. DI structures design at each target frequency based on different of m

Based on the equation in (7), the performance prediction of a PC can be possible. Optimized layouts with different m value can be compared to verify the theory of the present transverse PC structure. To test the effect of the value m , [Fig. 12\(a\)](#) shows the two designs optimized for 2 and 3 for m . As the destructive interference can be observed at the frequencies satisfying the equation in (7), it turns out that the optimized layouts are similar to each other. In [Fig. 12\(b\)](#), the enhanced attenuation performance of all TOPCs and effective operation at $m = 1, 2$, and 3 can be observed. First of all, this example indicates that the destructive interference phenomenon tailored at one single frequency can be observed for the other frequencies in (7). **Table 2** compares the objective values of the three designs. As illustrated, each design is the best design for the specified frequency.

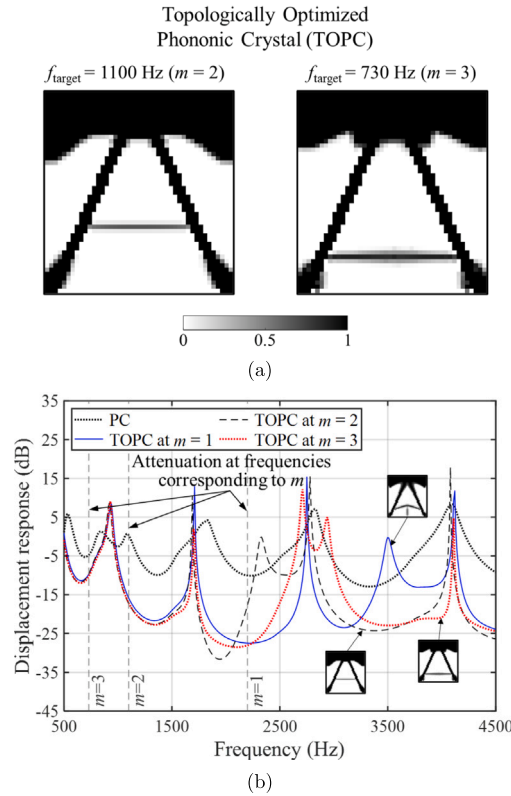


Fig. 12. (a) Layouts of TOPCs that $f_{\text{target}} = 1100 \text{ Hz}$, 730 Hz and (b) the displacement response curves of the PC and the TOPCs.

Table 2

Comparison of objective function values at each target frequency corresponding to m in the optimization results.

Frequency	Objective function value		
	TOPC at $m = 1$	TOPC at $m = 2$	TOPC at $m = 3$
2200 Hz ($m = 1$)	3.475×10^{-7}	2.307×10^{-5}	4.614×10^{-6}
1100 Hz ($m = 2$)	2.154×10^{-4}	1.691×10^{-4}	1.725×10^{-4}
730 Hz ($m = 3$)	7.692×10^{-4}	7.617×10^{-4}	7.118×10^{-4}

3.2. Example 2: DI structure design with a limited design domain

In the first example, it is observed that the mass at the top of the triangular structure plays an important role to attenuate the response. However, due to the limitation of space, it may be preferred to remove the proof mass. Therefore, to test the effect of the design domain, this subsection sets the design domain at the bottom of the structure as shown in Fig. 13.

Fig. 14(a) shows the optimized layout. Unlike in the first example, the two masses are attached at the two sides of the design domain and the triangular shape supporting structures are designed in this example. Altering the design domain leads to varied changes in the attenuation performance of the TOPC, as distinctly depicted in Fig. 14(b). The second example highlights the impact of the mass positioned at the top of the TOPC in the first example.

3.3. Example 3: Reinforcement design of DI structure

To explore the present destructive interference, the reinforcement design is considered in Fig. 15. In this reinforcement design, rather than designing an extended design, the optimal reinforcement design considered. In other words, the triangular shape structure pertains its shape and the reinforcement design is pursuit to improve the performance. To do this, the stiffness and the mass matrices in the design domain in Fig. 15 are re-formulated to consider the effect of reinforcement.

$$\mathbf{k}_e = (\gamma_e t_R + t_B) \mathbf{k}_{\text{nominal}}, \quad \mathbf{m}_e = (\gamma_e t_R + t_B) \mathbf{m}_{\text{nominal}} \quad (18)$$

where the basic structure thickness and the reinforcement thickness are denoted by t_B and t_R , respectively.

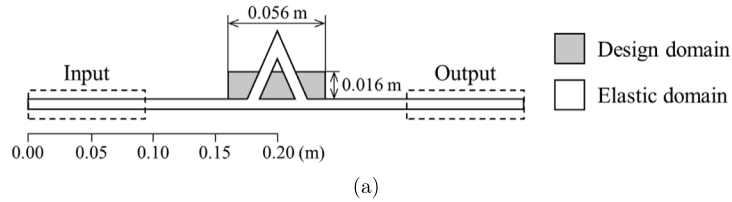


Fig. 13. Example 2: Optimization with the limited design domain.

Topologically Optimized Phononic Crystal (TOPC)
with limited design domain

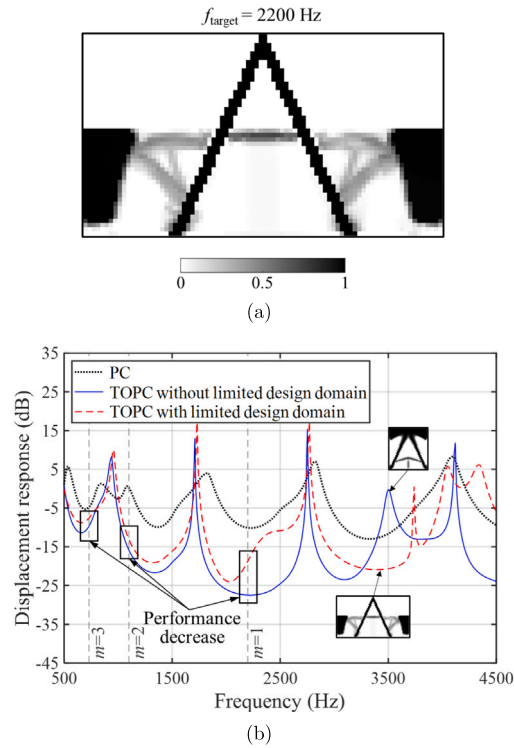


Fig. 14. (a) Layout of TOPC with limited design domain and (b) the displacement response curves of the PC and the TOPCs.

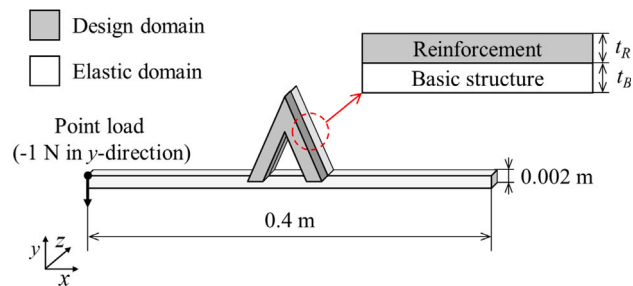


Fig. 15. Example 3: Design domain, geometric and boundary conditions of reinforcement design ($t_B = 0.005 \text{ m}$ and $t_R = 0.005 \text{ m}, 0.01 \text{ m}$ and 0.045 m).

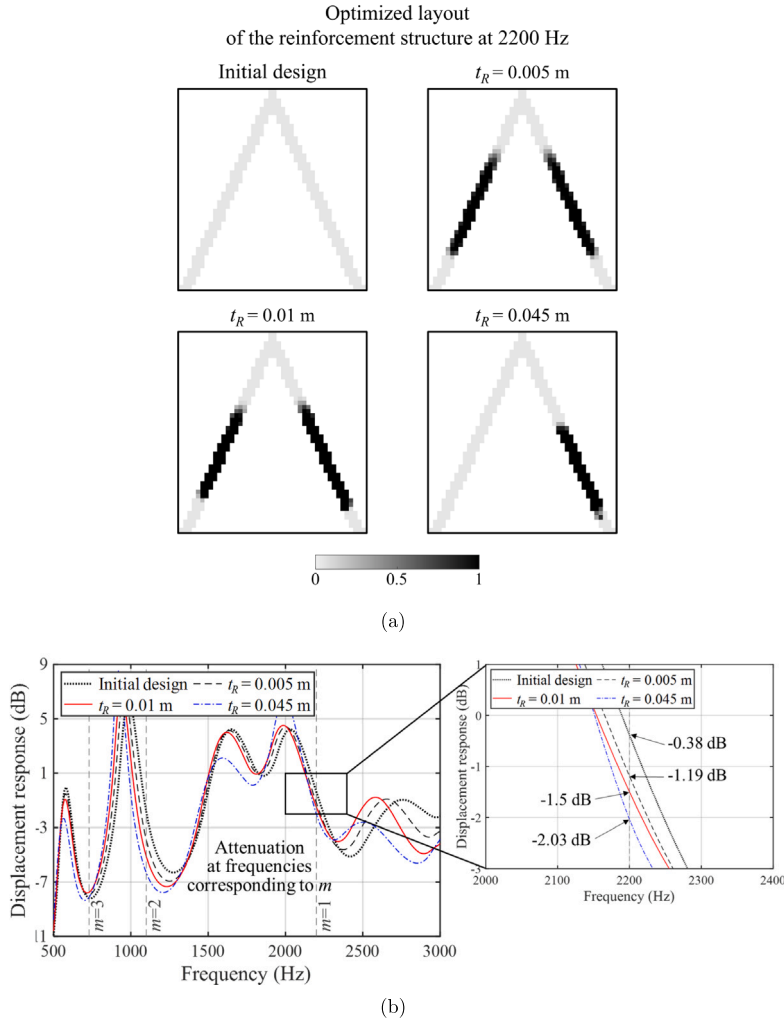


Fig. 16. (a) Layouts of the reinforcement structures that initial design ($t_R = 0$ m), $t_R = 0.005$ m, 0.01 m and 0.045 m and (b) the displacement response curves of these designs.

Fig. 16(a) shows the optimized reinforcements with several different reinforcement thickness values. Fig. 16(b) shows the responses of these reinforcement designs. These designs and the responses suggest that the straight parts of the destructive interference structure should be stiffer to improve the destructive interference. By increasing the thickness of the reinforcement, the performance is improved.

4. Conclusions

This study introduces an innovative topology optimization scheme aimed at enhancing the efficacy of the destructive interference (DI) structure. In our contribution, we presented the concept of the destructive interference structure for mitigating transverse mechanical waves and highlighted its potential effectiveness. Nevertheless, challenges arose due to mechanical resonance occurring in proximity to the target frequencies, hindering the effective suppression of transverse waves. To ameliorate the attenuation performance of the destructive interference structure, we employed a topology optimization approach. Through the identification of an optimized void-structure configuration within the design domain, the performance of the DI structure exhibited significant enhancements. In addition, the reinforcement design is also pursued through the topology optimization concept. The optimization results revealed valuable insights. First of all, the resonance of the DI structure shifts the phase of the mechanical wave. Thus, the topology optimization scheme can tune the resonance frequency shift. Secondly, by the topology optimization, the amplitude disparity of the two waves is minimized by the optimized layout that is crucial in the design of the destructive interference. Thirdly, to improve the performance of the DI structure, the loss of the elastic wave can be minimized by either strengthening the straight

parts or weakening the sharp junctions. For future research, the DI structure can be designed considering more complex mechanical waves.

CRediT authorship contribution statement

Tam Yee Ha: Writing – original draft, Visualization, Validation, Methodology, Investigation, Formal analysis, Conceptualization. **Gil Ho Yoon:** Writing – original draft, Validation, Supervision, Project administration, Methodology, Investigation, Conceptualization.

Declaration of competing interest

The authors declare that they have no known competing financial interests or personal relationships that could have appeared to influence the work reported in this paper.

Data availability

No data was used for the research described in the article.

Acknowledgments

This work was supported by the National Research Foundation of Korea (NRF) grant funded by the Korea government (MSIT) (No.2018R1A5A7025522).

References

- [1] H. Lv, X. Tian, M.Y. Wang, D. Li, Vibration energy harvesting using a phononic crystal with point defect states, *Appl. Phys. Lett.* 102 (3) (2013).
- [2] S. Tol, F.L. Degertekin, A. Erturk, Phononic crystal luneburg lens for omnidirectional elastic wave focusing and energy harvesting, *Appl. Phys. Lett.* 111 (1) (2017).
- [3] S.-H. Jo, H. Yoon, Y.C. Shin, B.D. Youn, A graded phononic crystal with decoupled double defects for broadband energy localization, *Int. J. Mech. Sci.* 183 (2020).
- [4] J. Zhao, B. Bonello, L. Becerra, O. Boyko, R. Marchal, Focusing of Rayleigh waves with gradient-index phononic crystals, *Appl. Phys. Lett.* 108 (22) (2016).
- [5] S. Mukherjee, S. Fabrizio, S. Gopalakrishnan, Phononic band gap design in honeycomb lattice with combinations of auxetic and conventional core, *Smart Mater. Struct.* 25 (5) (2016).
- [6] Y. Zhou, L. Ye, W. Chen, Impact mitigation performance of hybrid metamaterial with a low frequency bandgap, *Int. J. Mech. Sci.* 213 (2022).
- [7] L. D'Alessandro, E. Belloni, R. Ardito, A. Corigliano, F. Braghin, Modeling and experimental verification of an ultra-wide bandgap in 3D phononic crystal, *Appl. Phys. Lett.* 109 (22) (2016).
- [8] J.C. Guo, J.R. Li, Z. Zhang, Interface design of low-frequency band gap characteristics in stepped hybrid phononic crystals, *Appl. Acoust.* 182 (2021).
- [9] F. Casadei, J. Rimoli, M. Ruzzene, Multiscale finite element analysis of wave propagation in periodic solids, *Finite Elem. Anal. Des.* 108 (2016) 81–95.
- [10] Z. Jia, Y. Chen, H. Yang, L. Wang, Designing phononic crystals with wide and robust band gaps, *Phys. Rev. A* 9 (4) (2018) 044021.
- [11] J. Lou, L. He, J. Yang, S. Kitipornchai, H. Wu, Wave propagation in viscoelastic phononic crystal rods with internal resonators, *Appl. Acoust.* 141 (2018) 382–392.
- [12] G. Wen, H. Ou, J. Liu, Ultra-wide band gap in a two-dimensional phononic crystal with hexagonal lattices, *Mater. Today Commun.* 24 (2020) 100977.
- [13] Y. Sun, Y. Yu, Y. Zuo, L. Qiu, M. Dong, J. Ye, J. Yang, Band gap and experimental study in phononic crystals with super-cell structure, *Results Phys.* 13 (2019) 102200.
- [14] K. Sellami, H. Ketata, M.H. Ben Ghazlen, Locally resonant phononic crystals band-gap analysis on a two dimensional phononic crystal with a square and a triangular lattice, *Opt. Quantum Electron.* 51 (2019) 1–14.
- [15] X. An, H. Fan, C. Zhang, Elastic wave and vibration bandgaps in planar square metamaterial-based lattice structures, *J. Sound Vib.* 475 (2020).
- [16] V. Gupta, R.K. Munian, B. Bhattacharya, Dispersion analysis of the hourglass-shaped periodic shell lattice structure, *Int. J. Solids Struct.* 254–255 (2022).
- [17] W. Liu, G.H. Yoon, B. Yi, Y. Yang, Y. Chen, Ultra-wide band gap metasurfaces for controlling seismic surface waves, *Extreme Mech. Lett.* 41 (2020).
- [18] W. Liu, B. Yi, G.H. Yoon, H. Choi, Functionally graded phononic crystals with broadband gap for controlling shear wave propagation, *Adv. Eng. Mater.* 22 (12) (2020).
- [19] J. Xu, X. Zhang, R. Yan, Coupled piezoelectric phononic crystal for adaptive broadband wave attenuation by destructive interference, *J. Appl. Mech.* 87 (9) (2020).
- [20] J. Xu, G. Hu, L. Tang, Y. Zhang, R. Yan, Modeling and analysis of phononic crystal with coupled lanes for enhanced elastic wave attenuation, *J. Vib. Acoust.* 143 (2) (2021).
- [21] G.A. Gazonas, D.S. Weile, R. Wildman, A. Mohan, Genetic algorithm optimization of phononic bandgap structures, *Int. J. Solids Struct.* 43 (18–19) (2006) 5851–5866.
- [22] H.-W. Dong, X.-X. Su, Y.-S. Wang, Multi-objective optimization of two-dimensional porous phononic crystals, *J. Phys. D: Appl. Phys.* 47 (15) (2014).
- [23] Z. Zhang, Y. Fan Li, F. Meng, X. Huang, Topological design of phononic band gap crystals with sixfold symmetric hexagonal lattice, *Comput. Mater. Sci.* 139 (2017) 97–105.
- [24] A.K. Sharma, M. Kosta, G. Shmuel, O. Amir, Gradient-based topology optimization of soft dielectrics as tunable phononic crystals, *Compos. Struct.* 280 (2022).
- [25] G. Yi, B.D. Youn, A comprehensive survey on topology optimization of phononic crystals, *Struct. Multidiscip. Optim.* 54 (5) (2016) 1315–1344.
- [26] W. Liu, G.H. Yoon, B. Yi, H. Choi, Y. Yang, Controlling wave propagation in one-dimensional structures through topology optimization, *Comput. Struct.* 241 (2020).
- [27] S.L. Vatanabe, G.H. Paulino, E.C. Silva, Maximizing phononic band gaps in piezocomposite materials by means of topology optimization, *J. Acoust. Soc. Am.* 136 (2) (2014) 494–501.
- [28] K. Qiu, C. Fei, W. Zhang, Band-gap design of reconfigurable phononic crystals with joint optimization, *Mech. Adv. Mater. Struct.* (2022) 1–17.

- [29] G.H. Yoon, Structural topology optimization for frequency response problem using model reduction schemes, *Comput. Methods Appl. Mech. Engrg.* 199 (25–28) (2010) 1744–1763.
- [30] G.H. Yoon, Y.Y. Kim, The role of s-shape mapping functions in the simp approach for topology optimization, *KSME Int. J.* 17 (2003) 1496–1506.
- [31] B. Ahn, H. Lee, J.S. Lee, Y.Y. Kim, Topology optimization of metasurfaces for anomalous reflection of longitudinal elastic waves, *Comput. Methods Appl. Mech. Engrg.* 357 (2019) 112582.
- [32] J. Rong, W. Ye, Multifunctional elastic metasurface design with topology optimization, *Acta Mater.* 185 (2020) 382–399.
- [33] L.-Q. Chen, Analysis and control of transverse vibrations of axially moving strings, *Appl. Mech. Rev.* 58 (2) (2005) 91–116.
- [34] C. Ji, L. Yao, C. Li, Transverse vibration and wave propagation of functionally graded nanobeams with axial motion, *J. Vib. Eng. Technol.* 8 (2020) 257–266.
- [35] L.E. Kinsler, A.R. Frey, A.B. Coppens, J.V. Sanders, *Fundamentals of Acoustics*, John Wiley & Sons, 2000.
- [36] L. Wang, H. Hu, Flexural wave propagation in single-walled carbon nanotubes, *Phys. Rev. B* 71 (19) (2005) 195412.
- [37] S. Elliott, L. Billet, Adaptive control of flexural waves propagating in a beam, *J. Sound Vib.* 163 (2) (1993) 295–310.
- [38] K. Svanberg, MMA and GCMMA-two methods for nonlinear optimization, 2007, pp. 1–15, vol 1.
- [39] L. Shu, M.Y. Wang, Z. Fang, Z. Ma, P. Wei, Level set based structural topology optimization for minimizing frequency response, *J. Sound Vib.* 330 (24) (2011) 5820–5834.
- [40] M. Yulin, W. Xiaoming, A level set method for structural topology optimization and its applications, *Adv. Eng. Softw.* 35 (7) (2004) 415–441.
- [41] N.P. Van Dijk, K. Maute, M. Langelaar, F. Van Keulen, Level-set methods for structural topology optimization: a review, *Struct. Multidiscip. Optim.* 48 (2013) 437–472.
- [42] X. Zhang, A. Takezawa, Z. Kang, A phase-field based robust topology optimization method for phononic crystals design considering uncertain diffuse regions, *Comput. Mater. Sci.* 160 (2019) 159–172.
- [43] A. Takezawa, S. Nishiwaki, M. Kitamura, Shape and topology optimization based on the phase field method and sensitivity analysis, *J. Comput. Phys.* 229 (7) (2010) 2697–2718.
- [44] M.Y. Wang, S. Zhou, Phase field: a variational method for structural topology optimization, *Comput. Model. Eng. Sci.* 6 (6) (2004) 547–566.
- [45] J. Bai, W. Zuo, Hollow structural design in topology optimization via moving morphable component method, *Struct. Multidiscip. Optim.* 61 (1) (2020) 187–205.
- [46] W. Zhang, Y. Liu, Z. Du, Y. Zhu, X. Guo, A moving morphable component based topology optimization approach for rib-stiffened structures considering buckling constraints, *J. Mech. Des.* 140 (11) (2018) 111404.
- [47] W. Zhang, J. Song, J. Zhou, Z. Du, Y. Zhu, Z. Sun, X. Guo, Topology optimization with multiple materials via moving morphable component (MMC) method, *Internat. J. Numer. Methods Engrg.* 113 (11) (2018) 1653–1675.